MHD AND FAST PARTICLES IN TOKAMAKS

S.E. Sharapov

Euratom/CCFE Fusion Association, Culham Science Centre, Abingdon, Oxfordshire OX14 3DB, UK
Sergei.Sharapov@ccfe.ac.uk

ABSTRACT

An introduction is given to ideal MHD waves and the problem of resonant interaction between such waves and energetic ions born in fusion reactions and/or produced by auxiliary plasma heating. Shear Alfvén waves are shown to form a discrete spectrum of Global Alfvén Eigenmodes in current-carrying cylindrical plasmas and Toroidal Alfvén Eigenmodes in toroidal plasmas. A comparison between theory and experiment is presented for the observed discrete spectra of Alfvén waves driven by energetic ions in Joint European Torus. The mechanism of excitation of Alfvén instabilities is qualitatively explained by considering particle-to-wave power transfer, and mechanisms of wave-induced re-distribution and losses of energetic ions are discussed.

I. INTRODUCTION

Instabilities of Alfvén Eigenmodes (AEs)[1,2] are an important issue for burning plasma studies, with weakly-damped Toroidal Alfvén Eigenmode (TAE)[3] representing the most dangerous mode that may limit the pressure of energetic ions and cause fast ion losses. Since 3.5 MeV alpha-particles are born in fusion deuterium-tritium (DT) plasmas at a speed exceeding the Alfvén velocity, these alpha-particles may excite TAE via Landau resonance $V_{\|\alpha} = V_A$ if the power transfer from the alphas to the wave exceeds the wave damping by thermal plasma[4]. The Alfvén instability is driven by radial gradient of energetic particle pressure if the fast particles have energy high enough to resonate with Alfvén waves, and this instability cause a radial re-distribution of the energetic particles giving non-optimal heating profiles and energetic particle losses damaging the first wall. Without the energetic particles the modes are stable ideal magneto-hydrodynamic (MHD) waves. The present lecture describes discrete weakly-damped AEs in cylindrical and toroidal plasmas and the fast particle drive and AE-induced transport of the fast particles.

I.A. Fast ions in fusion plasmas

In present day experiments, energetic particles produced with auxiliary heating systems have very high parameters well suitable for investigating AEs with further extrapolation to burning plasmas with significant pressure of alpha-particles. On Joint European Torus (JET), energetic ions are produced with NBI and ICRH techniques capable of accelerating hydrogen isotopes H, D, T, and He^3 up to the MeV energy range[5,6]. It is also possible to accelerate a population of He^4 ions up to the MeV energy range with NBI+ICRH technique in helium plasma which has no fusion products[7]. Table I presents typical values of energetic ion populations achieved in JET experiments with ICRH, the values for alpha-particles in JET deuterium-tritium (DT) plasmas, and expected alpha-particle values in burning ITER plasma.

Table I. Characteristics of ICRH-accelerated ions and alpha-particles in JET and ITER: slowing down time, τ_S, heating power per volume at the magnetic axis, P_f (0), ratio of the on-axis fast ion density to electron density, n_f (0) / n_e(0), on-axis fast ion beta, β_f(0), volume-averaged fast ion beta, $\langle\beta_f\rangle$ (%), and normalised radial gradient of fast ion beta, max$|R\nabla\beta_f|$.

Reference	JET[5,6]	JET[7]	JET[8]	ITER[9]
Fast ions	H or He^3	He^4	Alpha	Alpha
Source	ICRH tail	ICRH tail	Fusion	Fusion
Mechanism	minority	3rd harm. of NBI	DT nuclear	DT nuclear
τ_S (s)	1-0.9	0.4	1.0	0.8
P_f (0) (MW/m^3)	0.8-1	0.5	0.12	0.55
n_f (0) /n_e(0) (%)	1-1.5	1.5	0.44	0.85
β_f (0) (%)	2	3	0.7	1.2
$\langle\beta_f\rangle$ (%)	≈0.3	0.3	0.12	0.3
max$\|R\nabla\beta_f\|$ (%)	≈5	5	3.5	3.8

I.B. Measuring Alfvén perturbations

Alfvénic instabilities are observed as high-frequency perturbations, having a typical frequency in the plasma reference frame from 50 to 500 kHz. The observed spectrum of the instabilities is not continuous, but discrete, with TAE in the range of 100-200 kHz in the plasma reference frame. Elliptical Alfvén Eigenmodes[10] are also seen sometimes at a frequency twice that of TAEs, and Alfvén Cascade eigenmodes[11] are seen in discharges with reversed magnetic shear at a frequency below the TAE frequency. The modes are detected by

external magnetic pick-up coils with a high sampling rate[8,12]. They can be also detected using interferometry[13], reflectometry[14], and electron cyclotron emission[11]. A typical magnetic spectrogram showing amplitude of magnetic perturbations as function of frequency and time is shown in Figure 1. Multiple TAE modes with different toroidal mode numbers are seen as a discrete spectrum in the frequency range 250-450 kHz in this plasma with high toroidal rotation that causes Doppler shift of frequency (to be described later). We'll try to understand why the spectrum of TAE is discrete and what limits the number of unstable TAE.

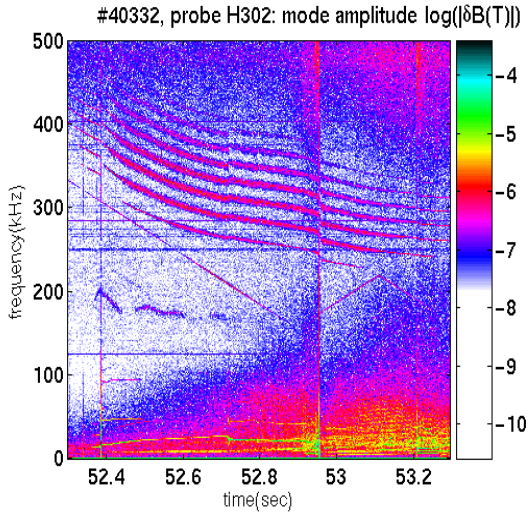

Fig.1. Magnetic spectrogram (Fourier decomposition as function of time) of a Mirnov coil signal.

II. MHD WAVES WITHOUT FAST PARTICLES

Plasma represents a self-consistent system of charged particles and perturbed electric and magnetic fields. For describing the plasma particles, we take into account the quasi-neutrality condition,

$$n_e = \sum_i Z_i \cdot n_i$$

and take velocity moments of kinetic Vlasov equations for electrons and ions and sum them to obtain

$$\frac{\partial \rho}{\partial t} + \nabla \cdot (\rho \mathbf{V}) = 0;$$

$$\rho \frac{d\mathbf{V}}{dt} = -\nabla p + \frac{1}{c}\mathbf{J} \times \mathbf{B};$$

$$\frac{\partial p}{\partial t} + \mathbf{V} \cdot \nabla p + \Gamma\ p \nabla \cdot \mathbf{V} = 0;$$

$$\mathbf{E} + \frac{1}{c}\mathbf{V} \times \mathbf{B} = 0;$$

where ρ and $\mathbf{V}$ are mass density and mass velocity of the plasma, p is plasma pressure, and Γ is adiabaticity index. This set of equations has no resistivity or other dissipative effects and described ideal magneto-hydrodynamics (MHD) evolution of plasma. For describing electromagnetic fields in the plasma, Maxwell's equations are used

$$\nabla \times \mathbf{B} = \frac{4\pi}{c}\mathbf{J};$$

$$\nabla \times \mathbf{E} = -\frac{1}{c}\frac{\partial \mathbf{B}}{\partial \mathbf{t}};$$

$$\nabla \cdot \mathbf{B} = 0.$$

For considering small linear perturbations of plasma near the equilibrium, all the field and plasma variables are represented as sums of equilibrium (denoted by subscript 0) and perturbed (denoted by δ) quantities as follows:

$$\mathbf{J} = \mathbf{J}_0 + \delta\mathbf{J},\ \mathbf{B} = \mathbf{B}_0 + \delta\mathbf{B},\ \mathbf{V} = \delta\mathbf{V},$$

$$p = p_0 + \delta p,\ \rho = \rho_0 + \delta\rho,\ \mathbf{E} = \delta\mathbf{E}, \qquad (1)$$

where all the perturbed quantities satisfy $\delta << 1$, i.e. $|\delta\mathbf{J}/\mathbf{J}_0| << 1$ etc. We assume the time-space dependence corresponding to waves, $\delta A \propto \exp(-i\omega t + ikr)$ in the limit $\omega << \omega_{Bi} \equiv e_i B_0 / mc$. One can now substitute the expressions (1) in the starting set of equations and obtain equations with terms: a) not having δ at all; b) having δ; c) having δ^2 etc. The terms not having δ are balanced due to the plasma equilibrium

$$\nabla p_0 = \frac{1}{c}\mathbf{J}_0 \times \mathbf{B}_0 \qquad (2)$$

and terms linear in δ describe ideal MHD perturbations:

$$\frac{\partial \delta\rho}{\partial t} + \nabla \cdot (\rho_0 \delta\mathbf{V}) = 0 \qquad (3)$$

$$\rho_0 \frac{d\,\delta\mathbf{V}}{dt} = -\nabla\,\delta p + \frac{1}{4\pi}[\nabla \times \delta\mathbf{B}] \times \mathbf{B}_0 \qquad (4)$$

$$\frac{\partial}{\partial t}\delta\mathbf{B} = \nabla \times [\delta\mathbf{V} \times \mathbf{B}_0] \qquad (5)$$

$$\delta p = \Gamma\ \frac{p_0}{\rho_0}\delta\rho\,. \qquad (6)$$

II.A. MHD waves in plasma

Introduce plasma displacement from the equilibrium, $\boldsymbol{\xi}$, related to $\delta\mathbf{V}$ via $\delta\mathbf{V} = \partial\boldsymbol{\xi}/\partial t$. From Eqs.(3), (5) we find

$$\delta\rho = -div(\rho_0 \boldsymbol{\xi})$$

$$\delta\mathbf{B} = \nabla \times [\boldsymbol{\xi} \times \mathbf{B}_0] = -\mathbf{B}_0 div\boldsymbol{\xi}_\perp + \mathbf{B}_0 \frac{\partial \boldsymbol{\xi}_\perp}{\partial z}$$

where $\nabla \times [\mathbf{a} \times \mathbf{b}] = (\mathbf{b}\nabla)\mathbf{a} - (\mathbf{a}\nabla)\mathbf{b} + \mathbf{a}\ div\,\mathbf{b} - \mathbf{b}\ div\,\mathbf{a}$ and $\mathbf{B}_0 \uparrow\uparrow \mathbf{e}_z$ were used. Substitute the expressions for $\delta\rho$, $\delta\mathbf{B}$ in the remaining two equations and obtain

$$\frac{\partial^2 \boldsymbol{\xi}}{\partial t^2} = c_S^2 \nabla div\boldsymbol{\xi} + V_A^2 \nabla_\perp div\boldsymbol{\xi}_\perp + V_A^2 \frac{\partial^2 \boldsymbol{\xi}_\perp}{\partial z^2}, \quad (7)$$

where $c_S^2 = \gamma\ p_0 / \rho_0$ is the ion sound speed, and $V_A^2 = B_0^2 / (4\pi\rho_0)$ is the square of Alfvén velocity. This equation describes linear MHD perturbations of homogeneous ideally conducting plasma. Single vector equation gives three scalar equations for three types of waves: compressional Alfvén and slow magnetosonic waves, in which the "returning" force are the magnetic pressure and the kinetic pressure, correspondingly, and the shear Alfvén wave, in which the "returning" force is the tension of magnetic field lines (see Figure 2).

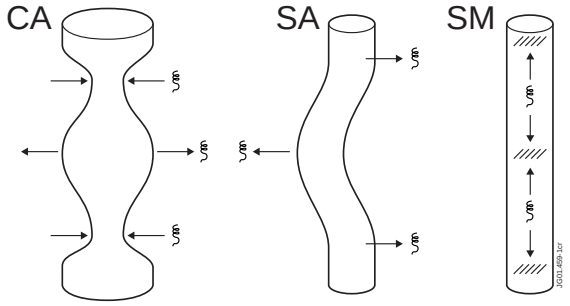

Fig.2. Plasma displacement ξ in three types of MHD waves[15]: Compressional Alfvén (CA), Shear Alfvén (SA), and Slow Magnetosonic (SM).

In contrast to the compressional waves, the shear Alfvén wave is incompressible:

$\xi_z = 0$,

$div\ \boldsymbol{\xi}_\perp = 0$.

For such waves the main MHD equation becomes simply

$$\frac{\partial^2 \boldsymbol{\xi}_\perp}{\partial t^2} = V_A^2 \frac{\partial^2 \boldsymbol{\xi}_\perp}{\partial z^2}, \quad (8)$$

which coincides with equation for string oscillations. The "returning" force is the tension of magnetic field lines, which act similarly to the strings. In shear Alfvén wave the fluid displacement vector $\boldsymbol{\xi}$ and $\delta\mathbf{E}$ are perpendicular to the magnetic field $\mathbf{B}_0$. The wave propagates along $\mathbf{B}_0$:

$$\omega = \pm k_\parallel V_A; \quad k_\parallel = \mathbf{k}\cdot\mathbf{B}_0 / B_0, \quad (9)$$

and it has no parallel perturbed components, $\delta E_\parallel = 0,\ \delta B_\parallel = 0$. In comparison to CA wave, SA wave requires less energy for excitation, and in comparison to SM wave, SA wave experiences less significant damping due to thermal ions since for typical plasmas $V_{Ti} / V_A = \sqrt{\beta_i} \approx 0.1 << 1$. As a result, the SA wave is easiest to excite, and this is why the SA wave constitutes the most significant part of the spectrum of MHD waves and is probably best studied.

The description of shear Alfvén waves above assumed homogeneous plasma. In spatially inhomogeneous plasmas with $V_A = V_A(r)$ and $k_\parallel = k_\parallel(r)$, the frequency of shear Alfvén waves, $\omega_A(r) = k_\parallel(r) \cdot V_A(r)$, varies with radius. A radially-extended packet of SA waves in such spatially inhomogeneous plasmas has a finite life time (which may be also interpreted as wave damping) since the radially different "slices" of the wave packet propagate at different velocities along different directions of $\mathbf{B}(r)$. As time increases, the "slices" of local Alfvén waves become thinner in radius and run into the short wavelength region, $k_r \to \infty$, where they are carried away due to the radial group velocity caused by finite Larmor radius (description of this effect goes beyond the scope of this lecture). The lifetime, τ, of the wave packet is inversely proportional to radial gradient of the local Alfvén frequency $\omega_A(r)$,

$$\tau \propto \left| \frac{d\,\omega_A(r)}{dr} \right|^{-1} \equiv \left| \frac{d}{dr} k_\parallel(r) \cdot V_A(r) \right|^{-1}.$$

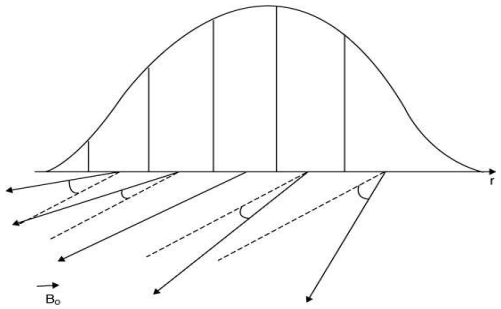

Fig.3. Schematic picture showing spread of a radially-extended wave-packet of shear Alfvén waves in inhomogeneous plasma.

The lifetime τ increases if the wave-packet is localised in vicinity of an extremum point of $\omega_A(r)$,

$$\frac{d}{dr}\omega_A(r)\Big|_{r=r_0} = 0. \quad (10)$$

It is of interest to investigate a possibility of existence of SA perturbations, which are localized in the vicinity of the Alfvén continuum extremum points and may be less damped and thus have a longer life-time.

II.B. Global Alfvén eigenmode (GAE) in cylindrical plasma with current

Investigations of Alfvén spectrum in cylindrical plasmas with plasma current and condition (10) fulfilled have

revealed that in cylindrical geometry, in addition to the continuous SA spectrum, $\omega^2 = \omega_A^2(r) \equiv k_\parallel^2(r) V_A^2(r)$, a discrete Global Alfvén Eigenmode (GAE) exists[16,17]. The mode was found as an extremely high-quality, Q ≡ ω/γ ~ 10^3, resonance excited in cylindrical plasma with co-directed equilibrium magnetic field and current by an external antenna. Figure 4 shows the plasma response seen as the antenna coil impedance as function of the frequency scanned in the antenna.

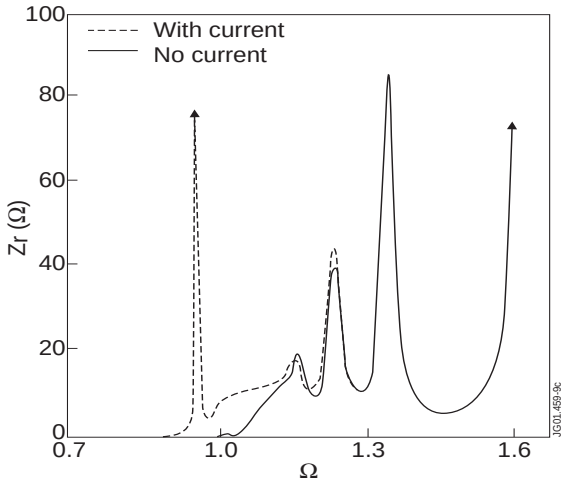

Fig.4. Real part of the coil impedance versus normalized frequency. GAE discrete eigenfrequency is shown with broken line as a high-quality narrow resonance peak below $\Omega = \omega / \omega_A^{\min} = 1$.

In cylindrical geometry, the length of the cylinder L determines the lowest parallel wave-vector as $k_\parallel^{\min} = 2\pi / L$ so that the lowest SA frequency is still above zero. The ideal MHD mode GAE with $0 < \omega_{GAE} < \omega_A^{\min}$ exists if the current profile provides a minimum in the Alfvén continuum via the condition:

$$\frac{1}{k_\parallel}\frac{dk_\parallel}{dr} = -\frac{1}{V_A}\frac{dV_A}{dr}.$$

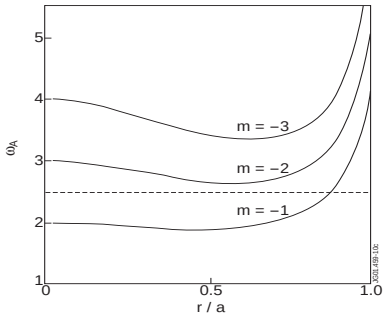

Fig.5. Structure of Alfvén continuum in cylindrical plasma with current and plasma density gradient.

It is important to note that the frequency of GAE is actually below the Alfvén continuum. This frequency shift is caused by the well-known property of electromagnetic waves (to which the SA wave belongs to) of forming a waveguide at the extremum of perpendicular refraction index. Indeed, the local minimum of the Alfvén continuum seen in Fig.5 provides a maximum of the perpendicular refraction index $N_r = ck_r / \omega$. Similarly to fiber optics, GAE propagating in a "wave-guide" surrounding the region of the extremum refraction index has most of the wave energy at the radial position of the extremum point. Figure 6 shows the radial structure of the GAE wave-fields.

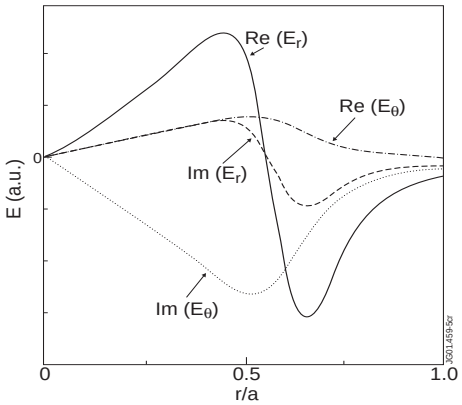

Fig.6. Radial structure of Global Alfvén Eigenmode with m=-2 in cylindrical plasma with current and density gradient.

Due to the frequency shift between GAE and $\omega_A^{\min}$, the eigenfrequency of GAE does not satisfy the local Alfvén resonance condition, i.e.

$$\omega_{GAE} \neq \omega_A(r) \tag{11}$$

Therefore, although GAE has all the properties of the SA wave, it represents a coherent radially-extended wave-packet, to which the phase mixing effect shown in Figure 3 does not apply, so GAE has no continuum damping.

II.C. Toroidal Alfvén Eigenmode (TAE)

In a torus, the wave solutions are quantized in toroidal and poloidal directions:

$$\phi(r,\vartheta,\zeta,t) = \exp(-i\omega t + in\zeta) \sum_m \phi_m(r) \exp(-im\vartheta) + c.c.$$

n is the number of wavelengths in toroidal direction and m is the number of wavelengths in poloidal direction. The parallel wave-vector for the m-th harmonic of a mode with toroidal mode number n, is determined by the safety factor $q(r) = rB_\zeta / RB_\vartheta$ as follows:

$$k_{\|m} = \frac{1}{R_0}\left(n - \frac{m}{q(r)}\right) \qquad (12)$$

It was found[3] that for a given $q(r)$ and n, but for different m two cylindrical SA branches become degenerate in toroidal geometry at radial positions

$$\omega = k_{\|m}(r)V_A(r) = -k_{\|m+1}(r)V_A(r), \qquad (13)$$

and so-called toroidicity-induced gap of the width $\Delta\omega/\omega \propto r/R_0$ exists at the frequency satisfying (13), with extremum points (10) caused by the toroidal coupling of neighboring poloidal harmonics m and $m+1$. In addition to the SA continuum, a new Toroidal Alfvén Eigenmode (TAE) was shown to exist in the TAE-gap. Figure 7 shows computed radial structure of Alfvén and SM continuous spectra in one of JET discharges, together with a discrete eigenfrequency corresponding to n=1TAE with eigenfrequency inside the TAE gap.

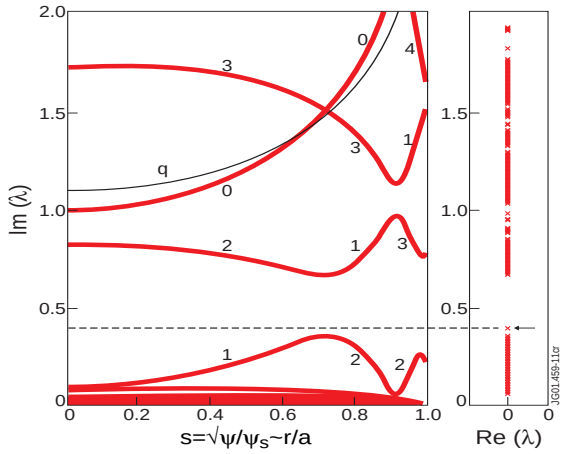

Fig.7. Radial structure of the Alfvén continuum in tokamak for toroidal mode number n=1.

Similarly to GAE in cylinder, TAE frequency does not satisfy the local Alfvén resonance condition in the region of TAE localization,

$$\omega_{TAE} \neq \omega_A(r)$$

so TAE does not experience strong continuum damping. Most of the wave energy of TAE with mode numbers n, m is localised at the position of the extremum where $k_{\|m}(r_{TAE}) = -k_{\|m+1}(r_{TAE})$, i.e.

$$q(r_{TAE}) = \frac{m+1/2}{n} \qquad (14)$$

as Figure 8 shows.

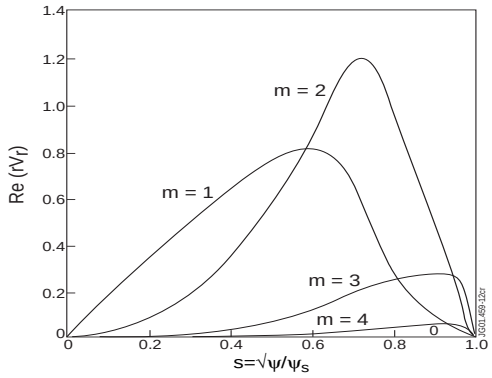

Fig.8. Radial structure of Toroidal Alfvén Eigenmode consisting of several coupled polidal harmonics.

We substitute this value of safety factor in (13) to obtain characteristic frequency of TAE,

$$\omega_{TAE} \cong \frac{V_A(r_{TAE})}{2R_0 q(r_{TAE})}, \qquad (15)$$

which does *not* depend on n or m. For typical plasma parameters on JET,

$$B_0 \cong 3\ T;\ n_i = 5\times10^{19}\ m^{-3};\ m_i = m_D;$$

one obtains $V_A \cong 6.6\times10^6\ m/s$, so that TAE frequency on JET ($R_0 = 3\ m$ and, e.g. $q \approx 1$) is:

$$\omega_{TAE} \cong 10^6\ \text{sec}^{-1};\ f_{TAE} \equiv \omega_{TAE}/2\pi \cong 160\ kHz.$$

We also note that the radial width of poloidal harmonic of TAE is

$$\Delta_{TAE} \approx r_{TAE}/m \approx r_{TAE}/nq.$$

Figure 9 shows experimentally observed TAE and EAE modes driven by ICRH-accelerated ions in one of JET discharges, together with computed TAE and EAE frequency gaps. At a low speed of toroidal rotation of the plasma, the frequencies in the plasma and laboratory reference frames are nearly the same, and the modeling of AE can be directly applied to the observation without the Doppler shift correction.

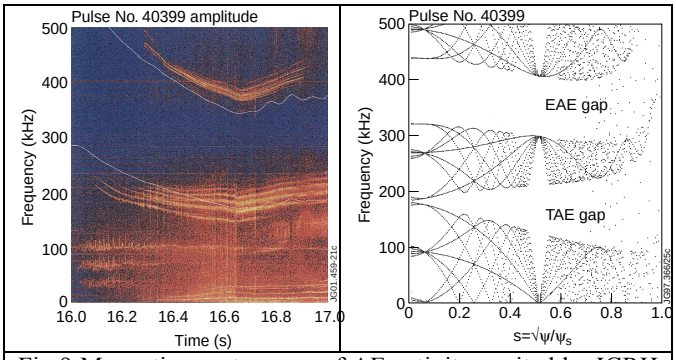

Fig.9 Magnetic spectrogram of AE activity excited by ICRH ions (left) and Alfvén continuum spectrum for n=1…6 as functions of radius (right)

In JET discharges with high power NBI, the uni-directional NBI spins up the plasma and drives a significant toroidal plasma rotation (up to 40 kHz). Frequencies of waves with mode number n in laboratory reference frame, f_n^{LAB}, and in the plasma, f_n^0, become different then and are related through the Doppler shift $nf_{rot}(r)$:

$$f_n^{LAB} = f_n^0 + nf_{rot}(r).$$

The Doppler shift proportional to the toroidal mode number explains why TAE are seen at much higher frequencies in Figure 1. Figure 10 shows an example of the observed and computed TAE modes in JET discharge with strong toroidal plasma rotation when the Doppler shift is included.

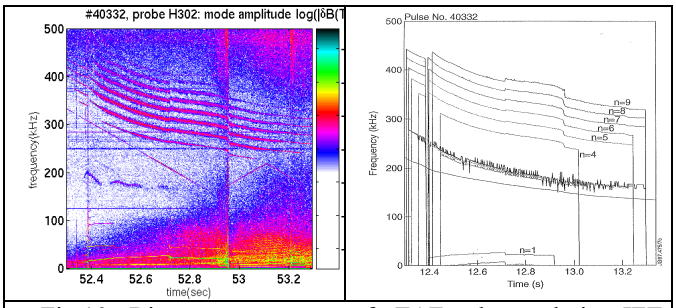

Fig.10 Discrete spectrum of TAE observed in JET discharge #40332. Plasma starts at t=40 sec (left) and eigenfrequencies of TAEs with n=4…9 computed for equilibrium in JET discharge #40332 (right).

III. TAE EXCITATION BY FAST PARTICLES

TAE modes have perturbed electric and magnetic field components, $\delta\mathbf{E}_\perp$, and $\delta\mathbf{B}_\perp$, perpendicular to the equilibrium magnetic field $\mathbf{B}_0$, but no parallel electric or magnetic fields. It is important to understand how such modes could be excited by energetic particles in toroidal geometry.

III.A. Qualitative explanation of the particle-to-wave power transfer

If some energetic ions move along $\mathbf{B}_0$ with velocity close to the phase velocity of the wave $\mathbf{V}_A$, the wave exchanges energy with such ions. For the ideal MHD shear Alfvén wave, it is the perpendicular electric field $\delta\mathbf{E}_\perp$ of the wave that interacts with the ions since, in toroidal geometry, the ions undergo the magnetic field curvature and ∇B drifts across the magnetic field. The drift surfaces of the energetic ions deviate from the magnetic surfaces to which the TAE mode is attached as shown schematically in Fig.11 for passing and trapped energetic ions.

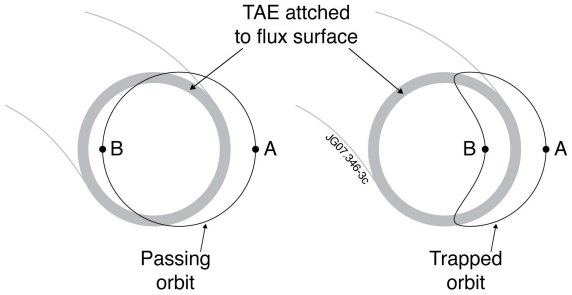

Fig.11 TAE modes are attached to magnetic flux surfaces, while energetic particles are not: they drift across the flux surfaces and TAE structure.

The exchange of energy between TAE and the ion occurs when the ion moves from, say, point A to point B across the radial structure of the mode and gains or loses energy $-e_h\Delta\varphi$, where, $\varphi(r)$ is electrostatic potential associated with the mode, and e_h is the charge of energetic ion labelled by subscript "h" (for hot ion). In the guiding centre approximation, the power transfer P_h from the ion to the mode is given by

$$P_h = -e_h \mathbf{v}_d \cdot \delta\mathbf{E}_\perp,$$

where $\mathbf{v}_d$ is unperturbed guiding centre drift velocity.

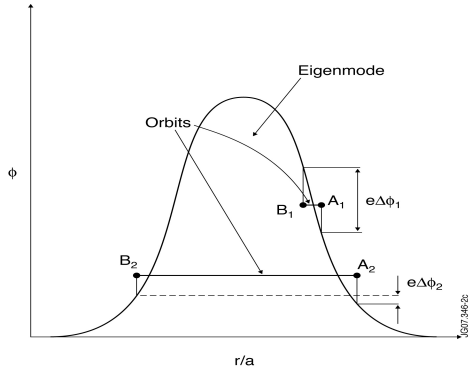

Fig.12 When charged particle moves radially across TAE from point A to point B, the mode and the particle exchange energy $e\Delta\phi$ as this Figure shows.

The particle-to-wave power transfer for the whole distribution function of energetic ions takes the form

$$P_h = \iint (-e_h \mathbf{v}_d \cdot \delta\mathbf{E}_\perp) f_h d^3v d^3x,$$

where f_h is the linear perturbed distribution function of hot ions. The most significant contribution to the power transfer comes from ions satisfying the wave-particle resonance, $\omega_0 - n\omega_\varphi - l\omega_\vartheta = 0$, where ω_φ and ω_ϑ are the toroidal and poloidal orbit frequencies of the energetic ions, and l is an integer.

Analytical estimates of the power transfer could be done in the reference frame of the energetic ion, which "sees" TAE electric field along its orbit as, e.g. a shifted circle in the simple case of the passing ions[19,18]:

$$r = \bar{r} + \Delta_O \cos\bar{\vartheta}\ ,$$

$$\vartheta = \bar{\vartheta} - \frac{\Delta_O}{\bar{r}}\sin\bar{\vartheta} \approx \bar{\vartheta}\ .$$

The structure of TAE electrostatic potential $\phi_m(r)$ in the reference frame of the ion could be expanded as,

$$\phi_m\left(\bar{r} + \Delta_O \cos\vartheta\right) = \sum_{l=0}^{\infty}\phi_{m,l}\cos l\vartheta$$

This poloidal dependence gives resonance conditions:

$$V_{\parallel} = \frac{V_A}{|1 - 2l|} = 1,\ \frac{1}{3},\ \frac{1}{5}\ldots$$

showing that TAE can interact with sub-Alfvénic ions at satellite resonances[2,18]. In the presence of gradients of the energetic particle distribution function, $\partial f_0/\partial r$ and $\partial f_0/\partial E$, and in the limit of the ion orbits smaller than the radial width of TAE, the expression for the normalized growth rate of TAE, γ , is given by

$$\frac{\gamma}{\omega_0} = \frac{P_h}{2W_{TAE}} \cong \beta_h\left(\frac{\omega_{*h}}{\omega_0} - 1\right)F\left(\frac{V_A}{V_h}\right),$$

where

$$\omega_{*h} = -\frac{m}{r}\frac{T_h}{e_h B}\frac{d\ln p_h}{dr}$$

is the diamagnetic frequency of the energetic ions, β_h, p_h, and T_h are the beta value, pressure, and temperature of the energetic ions, W_{TAE} is the wave energy of the mode, and function $F(V_A/V_h)$ depends on the type of energetic particle distribution function.

It is clear from Fig.12 that the particle-to-wave power transfer determined by the value $-e_h\Delta\varphi$ has a non-monotonic behavior as function of the ratio between drift orbit width and TAE width, so the power transfer achieves a maximum at $\Delta_O/\Delta_{TAE} \approx 1$[18] as Figure 13 shows

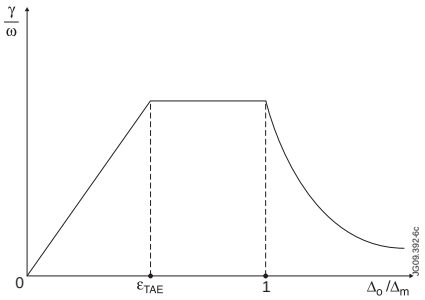

Fig.13. Qualitative graph showing how the power transfer depends on the ratio between fast particle drift orbit and radial width of TAE.

The net power transfer from energetic particles to the mode becomes positive if the radial gradient of the energetic particles is high enough to satisfy $\omega_{*h}/\omega_0 > 1$. The amplitude of the mode increases if the growth rate due to energetic particles exceeds TAE damping rate.

III.B. Experimental validation of TAE instability zone

One can observe experimentally how TAE modes are excited one-by-one at increasing pressure of energetic ions. Figure 14 shows JET discharge with gradually increasing power of ICRH driving TAE.

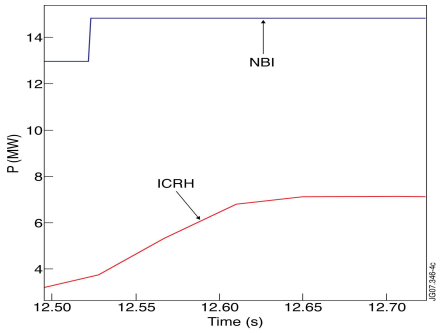

Fig.14. Power waveforms of ICRH and NBI in JET discharge # 40329.

As the population of ICRH-accelerated energetic ions increases, TAE modes with different toroidal mode numbers got excited one-by-one as Figure 15 shows. The instability starts from the most unstable TAE with $n = 8$ satisfying the maximum power transfer condition, $m \approx nq \approx r_{TAE}/\Delta_{orbit}$, and then involves more stable TAEs with other toroidal mode numbers at higher fast ion pressure.

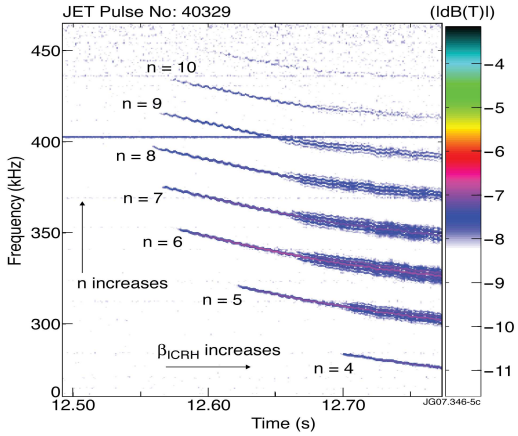

Fig.15. TAEs with different toroidal mode numbers appear one-by-one as fast ion pressure increases (JET discharge # 40329).

IV. TAE-INDUCED ENERGETIC PARTICLE TRANSPORT

Non-linearly the TAE instability leads to a radial flattening of the fast ion distribution function. However, losses of fusion born alphas must be minimized down to few percent (<5% on ITER[9]) for avoiding the first wall damage. Also, a radial redistribution of the alphas could give a non self-consistent alpha-heating profile and He ash profile and may affect the burn[21].

IV.A. Qualitative estimates

The unperturbed orbit of a charged particle is determined by three invariants:

$$\mu \equiv \frac{Mv_\perp^2}{2};\ E \equiv \frac{Mv^2}{2};\ P_\varphi \equiv -\frac{e}{c}\psi(r) + RMv_\varphi$$

In the presence of a fixed amplitude TAE, neither E nor P_φ is conserved for the ion orbit, but their combination is still invariant:

$$E - \frac{\omega}{n} P_\varphi = const$$

It is easy to see that a change in the ion energy is related to change in the ion radius induced by TAE as follows[22]:

$$\Delta E = \frac{\omega}{n}\Delta P_\varphi \cong \frac{\omega e}{nc}\psi' \Delta r \cdot$$

We can see then that the interaction between TAE and fast ions causes radial transport of the ions at nearly constant energy.

IV.B. Two main types of TAE-induced re-distribution and losses

In present-day machines, fast ion orbits are comparable to the machine radius, $\rho_\alpha / a \cong 10^{-1} \div 1$. A single-mode 'convective' transport linearly proportional to TAE amplitude $\propto \delta B_{TAE}$ is important as Figure 16 shows.

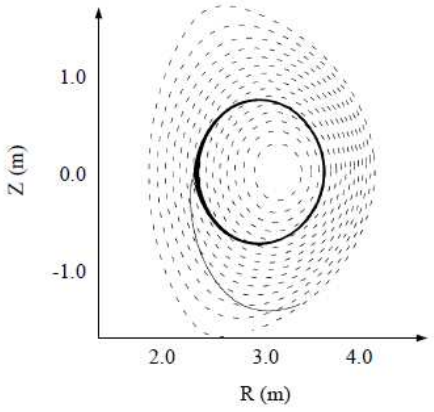

Fig.16. TAE-induced conversion of passing confined to a trapped lost ion on JET.

However, for ITER with parameter $\rho_\alpha / a \cong 10^{-2}$ the dominant channel of alpha-particle transport will differ from present-day machines. On ITER, higher-n (n > 10) TAEs will be most unstable. Under these conditions, a transport of alpha-particles is due to the wave-particle resonance overlap leading to a global stochastic diffusion, with the transport $\propto \delta B_{TAE}^2$. Figures 17 shows an example of stochastization of drift orbit surfaces and the resulting transport of alpha-particles computed for JET[22].

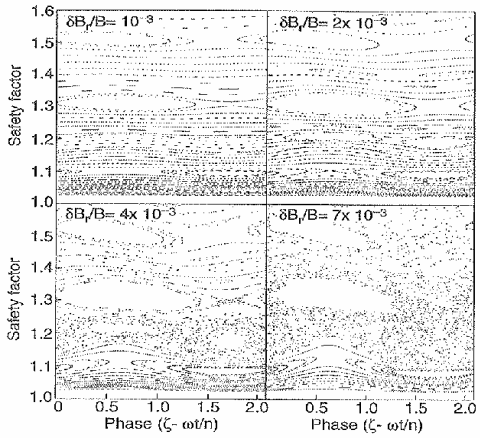

Fig.17. Stochastization of drift surfaces of fusion alpha-particles at increasing TAE amplitude.

REFERENCES

1. J. WESSON, *Tokamaks*, Clarendon Press, Oxford, 2011.
2. A.B. MIKHAILOVSKII, *Sov. Zh.ETPh.* **41** 890 (1975).
3. C.Z. CHENG, L. CHEN, M.S. CHANCE *Ann. Phys.* **161** 21 (1985).
4. G.Y. FU, J.W. VAN DAM *Phys. Fluids B* **1** 1949 (1989).
5. D.F.H. START et al., *Nucl. Fusion* **39** 321 (1999).
6. L.-G. ERIKSSON et al., *Nucl. Fusion* **39** 337 (1999).
7. M. MANTSINEN, *Phys.Rev.Lett.* **88** 105002 (2002).
8. S.E. SHARAPOV et al., *Nucl. Fusion* **39** 373 (1999).
9. A.FASOLI et al., *Nucl. Fusion* **47** S264 (2007).
10. R.BETTI, J.P.FREIDBERG, *Phys.Fl.* **B3** 1865 (1991).
11. S.E. SHARAPOV et al., *Phys. of Plasmas* **9** 2027 (2002).
12. A. FASOLI et al., *PPCF* **44** B159 (2002).
13. S.E. SHARAPOV *et al*., *Phys.Rev.Lett.* **93** 165001 (2004).
14. S. HACQUIN et al., *PPCF* **49** 1371 (2007).
15. B.B. KADOMTSEV, *Collective phenomena in plasmas*, Moscow: Nauka, 1976 (in Russian).
16. D.W. ROSS et al. *Phys. Fluids* **25** 652 (1982).
17. K.APPERT et al. *PPCF* **24** 1147 (1982).
18. B.N. BREIZMAN, S.E. SHARAPOV, *PPCF* **37** 1057 (1995).
19. H.L. BERK et al., *Phys. Lett.* **162A** 475 (1992).
20. D.T. SIGMAR et al., *Phys. Fluids* **B4** 1506 (1992).
21. H.L. BERK et al., *Phys. Fluids* **B5** 3969 (1993).
22. L.C. APPEL et al., *Nucl. Fusion* **35** 1697 (1995).